Numerical Heat Transfer, Part A, 59: 1–27, 2011

ISSN: 1040-7782 print/1521-0634 online
DOI: 10.1080/10407782.2010.523299

Taylor & Francis
Taylor & Francis Group

MODELING OF DIFFUSE CHARGE EFFECTS IN A MICROFLUIDIC BASED LAMINAR FLOW FUEL CELL

Isaac B. Sprague[1] and Prashanta Dutta[1,2]

[1]*School of Mechanical and Materials Engineering, Washington State University, Pullman, Washington, USA*

[2]*Department of Aerospace Information Engineering, Konkuk University, Seoul, Republic of Korea*

A mathematical model for laminar flow fuel cells including electrical double layer and ion transport effects is developed. The model consists of the Poisson-Nernst-Plank equations and the modified Navier-Stokes equations to account for the advection of species in the downstream direction. The generalized Frumkin-Butler-Volmer equation is used for the fuel cell kinetics. The finite-volume method is used to develop a system of algebraic equations from the governing partial differential equations, and a numerical algorithm is developed to obtain the results. The accuracy of the 2-D numerical simulation is validated against published results using a 1-D analytical solution. Numerical results show that the concentration distributions for both the neutral species and ions change in both the cross-stream and streamwise directions. An especially interesting result is the change in positive ion concentration within the electrical double layer along the streamwise direction. A study on the importance of the electric body force in the momentum conservation equations is also presented. It is found that the flow results are only affected by the electric body force term at the start of the electrodes and has a negligible impact on device performance results. This model allows us to study both kinetically active (electrodes) and inactive (insulated wall) regions for a microfluidic fuel cell. The mathematical model and numerical simulation will be particularly useful in analyzing the complex behavior that occurs in laminar flow electrochemical devices where a minimum of two spatial dimensions must be considered and the electrical double layer and ion transport cannot be neglected.

INTRODUCTION

Fuel cell technology has existed since 1839, when it was first introduced as a new way to produce electrical power from chemical energy. Fuel cells are electrochemical devices that combine fuel and oxidant sources to produce an electrical power. This is accomplished by separating a thermodynamically favorable reaction into two half reactions where ions are allowed to transfer from one half to the other through an electrolyte, while electrons are routed through a circuit. The half reactions are fuel oxidation at the anode and oxidant reduction at the cathode.

Received 12 February 2010; accepted 19 August 2010.

This research was partly supported by the 2010 KU Brain Pool Program of Konkuk University, Korea.

Address correspondence to Prashanta Dutta, School of Mechanical and Materials Engineering, Washington State University, Pullman, WA, 99164-2920, USA. E-mail: dutta@mail.wsu.edu

NOMENCLATURE

c	concentration, mM
C	normalized concentration
C_S	Stern layer capacitance, F
D	diffusion coefficient, m^2/s
e^-	electron
F	Faraday's constant, C/mol
i	current Iteration
I	total normalized current density
$J(\ )$	Jacobian matrix
j	current density, A/m^2
J	normalized current density
$\overleftarrow{k}$	oxidizing rate constant
$\overrightarrow{k}$	reducing rate constant
$\overleftarrow{K}$	normalized oxidizing rate constant
$\overrightarrow{K}$	normalized reducing rate constant
L	half channel height, m
m	number of control points
n	number of electrons involved in kinetic reaction
p	pressure, Pa
P	normalized pressure
r	number of sub-domains for parallel processing
R	ideal gas constant, $J/K \cdot mol$
$\vec{s}$	unknown vector
s	stoichiometric coefficient
S	normalized ionic current density
Sc	Schmidt Number, μ/D_E
T	absolute temperature, K
$\vec{v}$	fluid velocity vector, m/s
$\vec{V}$	normalized fluid velocity vector
x	position along channel, m
X	normalized position along channel
y	position across channel, m
Y	normalized position across channel
z	ion charge
α	kinetics symmetry factor
β	ratio of neutral species diffusion coefficient to ion diffusion coefficients
γ	ratio of electrolyte concentration to inlet concentration of neutral species
Γ	dimensionless parameter used in electric body force,$= \mu\omega_E/L^2C_E$
δ	ratio of Stern layer width to Debye length, λ_S/λ_D
$\Delta\phi_S$	potential drop across Stern layer, V
$\Delta\Phi_S$	normalized potential drop across Stern layer
ε	permittivity, F/m
$\vec{\eta}$	solution correction vector for Newton step
λ_D	Debye length, m
λ_S	width of Stern layer, m
μ	viscosity, $Pa \cdot s$
ξ	normalized inner length scale, $(y+L)/\lambda_D$
ρ	density, kg/m^3
ϕ	electrolyte potential, V
Φ	normalized electrolyte potential
ψ	electrode potential, V
Ψ	normalized electrode potential
ω	ion mobility, $m^2 \cdot mol/J \cdot s$

Subscripts

A	anion
An	anode
C	cation
Ca	cathode
Cell	device level values
E	electrolyte
El	electrode
F	fuel
in	inlet
O	oxidant
out	outlet
S	Stern layer

For example, in a polymer electrolyte membrane fuel cell, fuel oxidation produces positively charged ions and electrons which will be consumed by oxidant reduction at the cathode [1]. The anode and cathode are electrodes where charge transfer between the solid circuit and electrolyte can take place. The electrical double layer (EDL) forms at the interface of electrodes and electrolyte. The EDL is made up of the inner (Stern) layer and the outer (diffuse) layer and it plays a critical role in transfer of charge across an interface, such as electrons transferring from the fuel at the anode and to the oxidant at the cathode [2]. The resulting flow of electrons in an external circuit/load is the useable electrical power produced by the fuel cell.

Fuel cells have been studied in many forms and a common way to achieve the anode and cathode separation is through the use of a solid polymer electrolyte membrane [3–7]. However, a solid polymer electrolyte has a number of technical issues associated with it, such as cathode flooding and electrolyte dry-out as well as fabrication issues that are especially difficult at the micro level [8]. Recently, microfluidic technology has been introduced to eliminate polymer electrolyte membrane in a fuel cell [9]. This new electrochemical device is known as a laminar flow fuel cell (LFFC) where fuel and oxidant are allowed to flow at very low velocity in a microchannel. Colaminar flow is used to keep the fuel and oxidant streams separate, maintaining the separation between the anode and cathode half reactions. Figure 1 shows a schematic of a LFFC. Fuel and oxidant electrolyte streams are fed through different inlet channels to a main channel where they flow together but remain largely separated due to the nature of flow in a microchannel. There is some transverse diffusional mixing, which is depicted in Figure 1 as a growing wedge down the middle of the channel. However, as long as the fuel or oxidant do not cross over to the other electrode, the two half reactions are sufficiently isolated. In laminar flow fuel cells, positively charged ions and electrons are released from the fuel as it oxidizes at the anode. These positive ions migrate from the anode to the cathode through the flowing electrolyte stream in the channel and the electrons are routed to the cathode through an external electrical circuit (Figure 1). At the cathode the positive ions and electrons are consumed as the oxidant is reduced and a waste product is produced. This waste flows out of the channel along with the electrolyte stream to the waste reservoir.

The laminar flow fuel cell concept was first introduced in 2002 in the form of a vanadium redox cell with laminar flow separation [9]. The concept was further developed by studying different reactant solutions, flow rates, and individual electrode potentials to assess the performance limitations [10–12]. Several different incarnations of laminar flow fuel cells have been studied experimentally such as cells with an air breathing cathode electrode [13, 14], cells that utilize different configurations of graphite rods as electrodes [15], and cells that feed the reactants through porous electrodes [16] among others. While these devices were readily investigated

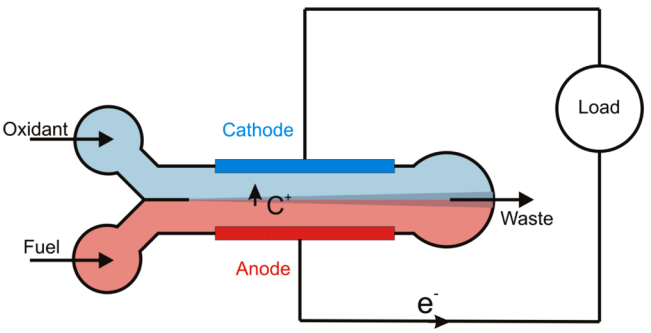

Figure 1. A basic representation of laminar flow fuel cell operation showing the separation of the fuel and oxidant streams. When fuel is oxidized at the anode ions are released, and travel across the channel to the cathode while the electrons move through the circuit thus forming useable current.

empirically, it is also of interest to study the fundamental behavior of devices through the use of mathematical models.

In the literature, there exist a number of models for laminar flow fuel cells. The simplest models use a constant electrode potential to model the reactant consumption along the channel. Bazylak et al. [17] used such a model to study fuel utilization for a variety of channel and electrode shapes and configurations. They also presented an innovative electrode design for improved fuel consumption. Multiple fuel feeds at various points along the electrode have also been studied using this type of model, and it was found that the effects of the depletion boundary layer could be minimized [18]. Device level models have also been presented previously. A laminar flow fuel cell using a Y-shaped microchannel has been studied using formic acid oxidation [19] and hydrogen peroxide decomposition [20], and a similar model was applied to a planar microchannel geometry [21].

The above-mentioned models assume that the electrolyte is electrically neutral throughout the channel and produce a linear electric potential gradient across the channel. Hence, these models simplify ionic transport in the electrolyte by using a charge conservation equation to model the electric field. These simplified models have two obvious limitations. First, they do not explicitly consider ion transport and its driving mechanisms such as electromigration. Second, they also neglect the EDL effects at the electrode–electrolyte interface which play a major role in the charge transfer kinetics at the interface as well as the overall cell potential [22, 23]. In order to capture these complex electrochemical phenomena, a more fundamental model is necessary.

A more general set of continuum equations that do not assume electroneutrality and include ion transport in electrochemistry are the Poisson-Nernst-Plank (PNP) equations. This model accounts for the strong coupling between the concentration of ions and the electric potential and has been used to model the ionic migration and the diffuse layer in electrochemical cells. Analytical solutions of the PNP equations without kinetics for the diffuse layer have been presented [24]. The charging of the EDL, a process essential to fuel cell operation, has also been studied numerically [25]. The Stern layer can be included as a mixed boundary condition to the PNP equations and has been used to show the importance of the double layer in interfacial kinetics [26] as well as in the time-dependent response to applied cell voltage [27]. Moreover, advanced models have been developed that account for the EDL and ion transport [28, 29] specifically for polymer electrolyte membrane fuel cells [30] and solid oxide fuel cells [31]. Thus far, the effects of the diffuse layer on electrochemical kinetics have only considered in solid electrolytes or stationary liquid electrolytes, and have never been considered for a flowing electrolyte or laminar flow fuel cells.

In this work, a mathematical model is developed for a LFFC which can be used to study the operational behavior of such devices. The model is based on the fundamental phenomena that govern the fluid flow, ion transport and electric potential in LFFC. Any such model would be able to capture the EDL and flow effects in electrochemical kinetics. This new model is able to use the more accurate generalized Frumkin-Butler-Volmer equation for kinetics by using the local concentration of reactants at the Stern layer-diffuse layer interface and the potential drop across the Stern layer. Here, the term ''generalized'' refers to the broad applicability of

this kinetic formulation that is not limited by assumptions such as equilibrium at the electrolyte-electrode interface or electroneutrality [28].

The model presented is a general variant of the Poisson-Nernst-Plank equations, where the Nernst-Plank equations will include the advection term which captures the species transport due to the bulk flow of the electrolyte. The equations are solved in two dimensions which is necessary for the prediction of basic LFFC phenomena such as the laminar separation and depletion boundary layer, or the local decrease in reactant concentration along the electrodes as it is consumed. The model input presented is the electrode potentials (Ψ_{An} and Ψ_{ca}), and and the cell current density I_{cell} can be recovered from the generalized Frumkin-Butler-Volmer electrode kinetics. Therefore, the model will be able to produce standard fuel cell metrics such as voltage-current plots.

GOVERNING EQUATIONS

Figure 2 shows the computational domain used for this work. We considered a planar microchannel with two inlet streams merging at the entrance ($x = 0$). For computational simplicity, it is assumed that the flow becomes fully developed within 2 L. Therefore, the outlet condition is set at $x_{\text{out}} = 2L$; however, the model is applicable for any domain size or aspect ratio. The electrodes are on the top and bottom channel walls and they begin at $x = x_{El}$ and end at the channel outlet, $x = x_{\text{out}}$. For simplicity, only two species, fuel (F) and oxidant (O), were considered for a redox reaction in the presence of a binary electrolyte consisting of a cation (C) and an anion (A) with a charge of $z_C = -z_A = 1$. Fuel is oxidized at the anode, and frees cation(s) and electron(s) which are then consumed at the cathode along with the

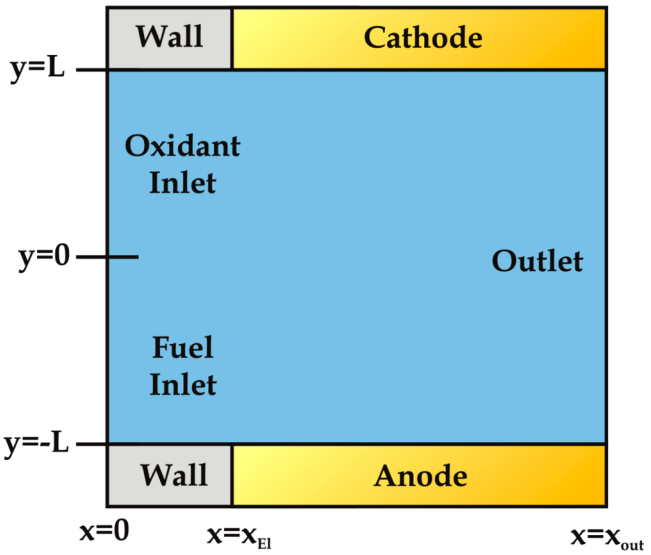

Figure 2. The computational domain considered for the model depicting a main channel with two inlet streams. Anode and cathode reaction regions starts at $x = x_{El}$.

oxidant to produce current. Therefore, the stoichiometric equations for the half reactions at the electrodes become

$$\text{Anode} : s_F \cdot F \rightarrow s_C \cdot C + n \cdot e^- \tag{1a}$$

$$\text{Cathode} : s_C \cdot C + n \cdot e^- + s_O \cdot O \rightarrow \text{waste} \tag{1b}$$

and the overall redox reaction becomes

$$\text{Overall} : s_F \cdot F + s_O \cdot O \rightarrow \text{waste} \tag{1c}$$

The parameter n represents the number of electrons released by fuel oxidation and consumed by oxidant reduction. Its value depends on type of fuel used in the overall reaction, i.e., for hydrogen $n = 2$ and for methanol $n = 6$. The stoichiometric coefficient, s, is the number of molecules of a given species that react with n electrons. The rate at which the half reactions proceed is governed by the generalized Frumkin-Butler-Volmer equation.

$$\text{Anode} : j = Fn\overleftarrow{k_{An}}\, c_F e^{(1-\alpha)\Delta\phi_s zF/RT} - Fn\overrightarrow{k_{An}}\, c_c e^{-\alpha\Delta\phi_s zF/RT} \tag{2a}$$

$$\text{Cathode} : j = Fn\overleftarrow{k_{Ca}}\, e^{(1-\alpha)\Delta\phi_s zF/RT} - Fn\overrightarrow{k_{Ca}}\, c_o c_c e^{-\alpha\Delta\phi_s zF/RT} \tag{2b}$$

where the concentration terms for the reactants are obtained from the continuum distribution of the concentration fields c_F, c_O, and c_C taken at the electrode of interest. It should be noted that the EDL will have significant impact on the value of c_C at the electrode. For simplicity the waste product was not considered in this work, but one could easily include a waste species by solving an additional concentration equation. In fact there are situations where accounting for the waste product is not necessary, such as if the cathode reaction were the oxygen reduction reaction. Then the product of the reaction would be water which is adsorbed into the bulk solution at a constant chemical potential for an aqueous solution. Depending on the reactions studied, the LFFC model presented can easily accommodate additional species.

Inspection of Eq. (2) reveals that the electrode kinetics is the difference between the oxidation current and reduction current at the electrode. This makes the rate constants critical to the operation of a fuel cell. Assume, for now, that the electrodes are not connected via an external electrical circuit/load so no charge is allowed to transfer between them. This condition is known as the open circuit case of a fuel cell for which the cell voltage is highest. Since no charge is allowed to transfer between the electrodes, the net current at each electrode must be equal to zero. If the oxidation and reduction rate constants were equal, then the value of $\Delta\phi_s$ for which the oxidation and reduction current are equal is zero. This would mean the total cell voltage would be zero at open circuit. However, if at the anode for example the reduction rate constant is less than the oxidation rate constant, then some negative value of $\Delta\phi_s$ would be required to achieve zero net current yielding a non-zero cell voltage. This negative value of $\Delta\phi_s$ requires the anode voltage to be negative and gives the fuel cell a cell voltage greater than zero. Therefore, the imbalance in rate

constants is fundamental to the fuel cell device and the selection of which can greatly impact the behavior of a cell.

The concentration distributions for the fuel (F) and oxidant (O) as well as the electrolyte components (cation C and anion A) are governed by the steady state transport equations.

$$\nabla \cdot (\vec{v}c_F) = \nabla \cdot (D_F \nabla c_F) \tag{3a}$$

$$\nabla \cdot (\vec{v}c_O) = \nabla \cdot (\mathrm{D}_O \nabla c_O) \tag{3b}$$

$$\nabla \cdot (\vec{v}c_C) = \nabla \cdot (D_C \nabla c_C + z_C \omega_C F c_C \nabla \phi) \tag{3c}$$

$$\nabla \cdot (\vec{v}c_A) = \nabla \cdot (D_A \nabla c_A + z_A \omega_A F c_A \nabla \phi) \tag{3d}$$

where ω is ionic mobility and is related to diffusion coefficient by $D = RT\omega$. The advection term, on the left-hand side of Eq. (3), indicates that the velocity of the fluid flow impacts the concentration distribution of a given species. This term has typically been neglected by previous solutions of the Poisson-Nernst-Plank equations.

The first term on the right-hand side of Eq. (3) shows the contribution of diffusion in the transport process. The coupling between ion transport in the electrolyte and the potential in the electrolyte is apparent from the second term on the right-hand side of Eqs. (3c) and (3d). This electromigration term states that the flux of a charged ion due to migration is proportional to the potential gradient. The potential in the electrolyte is coupled to the ion concentration through the Poisson's Equation:

$$-\nabla \cdot (\varepsilon_E \nabla \phi) = z_C F c_C + z_A F c_A \tag{4}$$

From this equation it is apparent how the potential in the electrolyte is coupled to the concentration distribution of the ions. The right-hand side is known as the charge density, and it becomes zero in the bulk fluid region (away from the electrode). However, near the electrodes the charge density will not be equal to zero and the electroneutrality condition is no longer valid.

The velocity field of the incompressible fluid can be obtained by solving the momentum and mass conservation equations [32].

$$\rho(\vec{v} \cdot \nabla)\vec{v} = \nabla \cdot (\mu \nabla \vec{v}) - \nabla p - (z_C F c_C + z_A F c_A)\nabla \phi \tag{5a}$$

$$\nabla \cdot \vec{v} = 0 \tag{5b}$$

The last term of Eq. (5a) is due to the electric body force (EBF) which is a function of the electric field and charge density.

Boundary Conditions

For a 2-D planar microchannel, there exist six different kinds of boundaries: fuel inlet, oxidant inlet, wall, anode electrode, cathode electrode, and outlet. Hence, six sets of boundary conditions are required for each unknown variable. The inlet streams provide a specified concentration for each species. The fuel inlet specifies the fuel concentration and has no oxidant influx and vice versa for the oxidant inlet. It is assumed that at the inlet the potential has an insulation condition. Therefore the boundary conditions for the electrochemical governing equations at the fuel inlet are

$$c_C = c_A = c_E \tag{6a}$$

$$c_F = c_{F,\text{in}} \tag{6b}$$

$$c_O = 0 \tag{6c}$$

$$\frac{\partial \phi}{\partial x} = 0 \tag{6d}$$

and at the oxidant inlet are

$$c_C = c_A = c_E \tag{7a}$$

$$c_O = c_{O,\text{in}} \tag{7b}$$

$$c_F = 0 \tag{7c}$$

$$\frac{\partial \phi}{\partial x} = 0 \tag{7d}$$

At the outlet it is assumed that the phenomenon is fully developed and therefore are no longer functions of the x direction. This translates to the assumption that there are no concentration gradients along the channel axis and there is no change in electrolyte potential.

$$\frac{\partial c_C}{\partial x} = \frac{\partial c_A}{\partial x} = \frac{\partial c_F}{\partial x} = \frac{\partial c_O}{\partial x} = 0 \tag{8a}$$

$$\frac{\partial \phi}{\partial x} = 0 \tag{8b}$$

The channel wall, in the absence of an electrode, provides a zero flux condition for the mass transport equations. It is also assumed that the wall is an insulator and has no surface charge yielding a zero potential gradient normal to the surface [32]. As a result the boundary conditions at the wall are

$$D_C \frac{\partial c_C}{\partial y} - z_C \omega_C F c_C \frac{\partial \phi}{\partial y} = 0 \tag{9a}$$

$$D_A \frac{\partial c_A}{\partial y} - z_A \omega_A F c_A \frac{\partial \phi}{\partial y} = 0 \tag{9b}$$

$$D_F \frac{\partial c_F}{\partial y} = 0 \tag{9c}$$

$$D_O \frac{\partial c_O}{\partial y} = 0 \tag{9d}$$

$$\frac{\partial \phi}{\partial y} = 0 \tag{9e}$$

The electrodes are the most important part of a fuel cell where interesting electrochemical interactions occur, and are of paramount importance for fuel cell operation. At the electrodes, the non-reacting species have a zero flux condition, while the reacting species have a flux equal to the ionic current density which is related to the electric current density by the Faraday constant, number of cations involved in the reaction and a stoichiometric coefficient derived from the reaction equations (Eq. (1)). The sign of the flux is determined by the species position in the stoichiometric equation, i.e., negative if the species is a reactant and positive if the species is a product. Therefore, for the mass transport equations, the anode boundary conditions are

$$D_C \frac{\partial c_C}{\partial y} - z_C \omega_C F c_C \frac{\partial \phi}{\partial y} = \frac{s_C j}{nF} \tag{10a}$$

$$D_A \frac{\partial c_A}{\partial y} - z_A \omega_A F c_A \frac{\partial \phi}{\partial y} = 0 \tag{10b}$$

$$D_F \frac{\partial c_F}{\partial y} = -\frac{s_F j}{nF} \tag{10c}$$

$$D_O \frac{\partial c_O}{\partial y} = 0 \tag{10d}$$

For the electrolyte potential at the boundary, an adaptation of the Stern model for the inner layer is used [26]. Here, the boundary value is determined by the electrode potential plus the drop across the Stern layer, $\phi = \psi + \Delta\phi_S$, where the potential is assumed to be linear and continuous with the potential in the electrolyte. The Stern layer thickness is determined by the ratio of the permittivity in the Stern layer over the capacitance of the Stern layer. For the anode electrode, the boundary condition for electrolyte potential is

$$\phi = \psi_A + \frac{\varepsilon_S}{C_S} \frac{\partial \phi}{\partial y} \tag{10e}$$

Similarly the boundary conditions for cathode (electrode) are

$$D_C \frac{\partial c_C}{\partial y} - z_C \omega_C F c_C \frac{\partial \phi}{\partial y} = -\frac{s_C j}{nF} \tag{11a}$$

$$D_A \frac{\partial c_A}{\partial y} - z_A \omega_A F c_A \frac{\partial \phi}{\partial y} = 0 \tag{11b}$$

$$D_F \frac{\partial c_F}{\partial y} = 0 \tag{11c}$$

$$D_O \frac{\partial c_O}{\partial y} = -\frac{s_O j}{nF} \tag{11d}$$

$$\phi = \psi_c + \frac{\varepsilon_s}{c_s} \frac{\partial \phi}{\partial y} \tag{11e}$$

It should be noted that the drop across the Stern layer will be negative for the anode and positive for the cathode except in the case of very low cell potentials.

The boundary conditions for momentum and mass conservation equations are straightforward. We assumed a fully developed velocity distribution in both fuel and oxidant inlet channels and therefore prescribed the fluid velocity profile as parabolic flow at each inlet. There exists a no slip and no penetration boundary conditions at the wall and electrodes. Finally, the pressure is specified as zero gauge at the outlet.

$$\text{Inlet} : \vec{v} = \vec{v}_{\text{in}} = v_{\max} \left[1 - \left(\frac{2(|y| - L/2)}{L} \right)^2 \right] \cdot \vec{i} + 0 \cdot \vec{j} \tag{12a}$$

$$\text{Outlet} : p = 0 \tag{12b}$$

$$\text{Walls} : \vec{v} = 0 \tag{12c}$$

NUMERICAL TECHNIQUE

The governing equations used to describe the laminar flow fuel cell are nonlinearly coupled, and hence for a two dimensional domain the systems of equations must be solved numerically. In this study the finite volume method is used to form algebraic equations. One of the major advantages of the finite volume method is the conservation of the parameter across the domain [33].

Since the fluid flow equations (Eq. (5)) are influenced by the parameters solved in Eqs. (3) and (4) they must be solved in conjunction with Eqs. (3) and (4). This was accomplished iteratively by solving Eq. (5) followed by Eqs. (3) and (4) until both results converged. For this work, the colocated semi-implicit method for pressure-linked equations (SIMPLE) algorithm is used to solve the flow equations [33, 34]. The system of equations used to describe electrochemical system (Eqs. (3) and (4)) is also nonlinear and highly coupled. Therefore, use of finite-volume method provides a set of nonlinear algebraic equations that are difficult to solve using tridiagonal matrix algorithm (TDMA). In this work Newton's method is applied

for a system of equations which is solved with a block TDMA. For this study, a parallel algorithm is developed to solve both flow and electrochemical equations concurrently (see Appendix 1). By implementing a parallel solver, significant computational time savings can be obtained. In this work, an Intel Core i7–975 3.33 GHz processor with four cores was used. The numerical results were completed in 4.72 h using four threads, while it took 12.5 h for a single thread.

MODEL VALIDATION

It is important to validate the accuracy of the numerical results if analytical/experimental results exist. Unfortunately, there is no analytical solution for the 2-D LFFC system presented in this study. Hence, we have obtained 1-D numerical solution from this 2-D model to compare with existing 1-D analytical results. In order to obtain

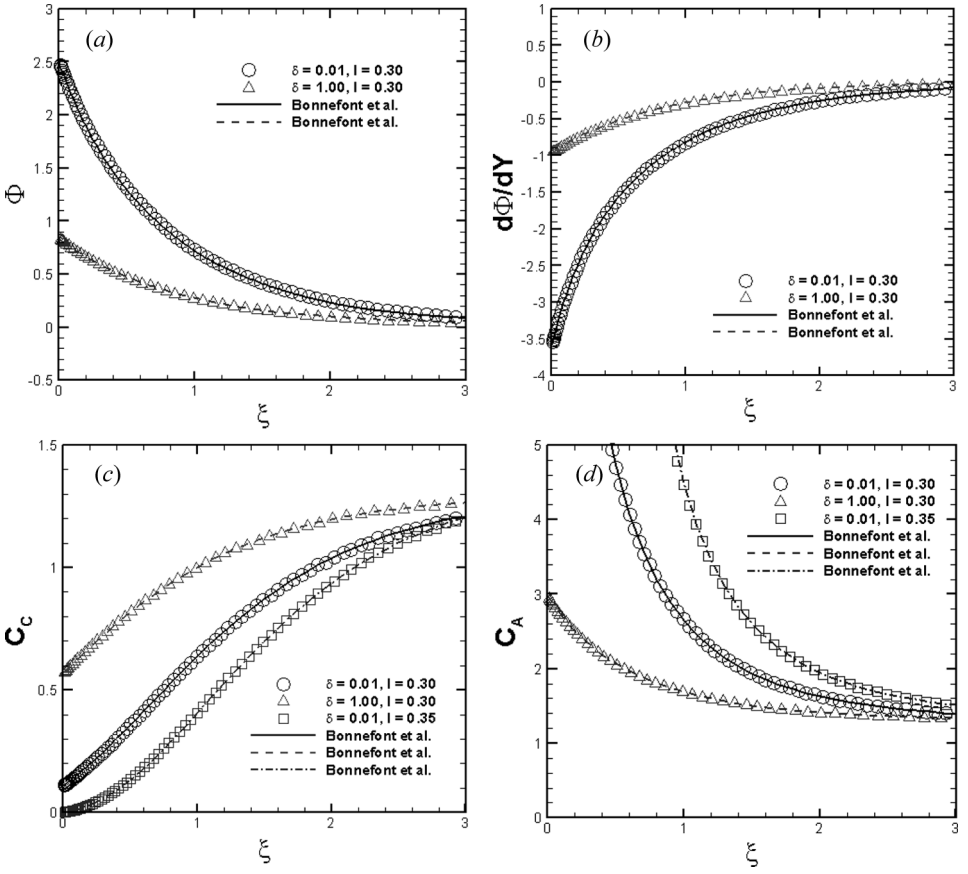

Figure 3. Numerical recreation of published analytical results validating the accuracy of the model and solution. The lines are the analytical results presented by Bonnefont et al. [26], while the symbols are the numerical results for the different scenarios; ○ is $\delta = 0.01$ and $I = 0.3$, and △ is $\delta = 1$ and $I = 0.3$, □ is $\delta = 0.01$ and $I = 0.35$. The results compared are (*a*) potential in the electrolyte, (*b*) the first derivative of potential with respect to Y, (*c*) the concentration distribution of the cation, and (*d*) the concentration distribution of the anion.

the 1-D results, the boundary conditions of the 2-D numerical model had to be changed and advection had to be neglected. At the inlet and outlet, potential was given an insulated condition and it was assumed there are no concentration gradient (same as equation 8). The electrodes were extended from $X=0$ to $X=2$, and the boundary conditions were the same as Eqs. (10) (anode) and (11) (cathode). To provide a Dirichlet condition for concentration, the concentration was prescribed for the center control points where $Y=0$. The electrolyte potential did not require a Dirichlet condition as the mixed boundary conditions at the electrodes provide a unique solution. Figure 3 compares 1-D numerical results with the existing analytical results for potential in the electrolyte, the first derivative of potential in the electrolyte, concentration of the cation, and concentration of the anion [26]. The results are presented against the normalized inner length scale which is defined as $\xi=(y+L)/\lambda_D$, where λ_D is the Debye length. In the figure, the lines represent the analytical solution and the symbols show the numerical results. Like Bonnefont et al. [26], for the case of $I=0.35$ only $\delta=0.01$ is presented for the concentration profiles, where $\delta=\lambda_S/\lambda_D$. Figure 3 shows excellent agreement between numerical results and published analytical solution validating the numerical model.

RESULTS AND DISCUSSION

For universal applicability, all numerical results are presented in normalized form. A brief description of our normalization technique and normalized variables are presented in Appendix 2 and Table 1, respectively. A laminar flow fuel cell operating under partial load, away from open or short circuit, with flowing electrolyte

Table 1. Definition of dimensionless parameters

Dimensional variable	Scale factor	Dimensionless variable
c_A	c_E	C_A
c_C	c_E	C_c
c_F	$c_{F,in}$	C_F
c_O	$c_{O,in}$	C_O
J	$D_E F_Z c_E/L$	J
$\overleftarrow{k_{An}}$	D_E/L	$\overleftarrow{k_{An}}$
$\overrightarrow{k_{An}}$	D_E/L	$\overrightarrow{k_{An}}$
$\overleftarrow{k_{Ca}}$	$c_E D_E/L$	$\overleftarrow{k_{Ca}}$
$\overrightarrow{k_{Ca}}$	D_E/Lc_E	$\overrightarrow{k_{Ca}}$
p	$\mu D_E/L^2$	P
$\vec{v}$	D_E/L	$\vec{V}$
x	L	X
y	L	Y
ϕ	RT/zF	Φ
ψ	RT/zF	Ψ

The dimensionless variable can be obtained by dividing the dimensional variable with the scale factor.

is considered. For the numerical results, the electrode potentials are set as $\Psi_{ca} = -\Psi_{an} = 3$, the kinetic rate constants are $K_{An} = 5 \times 10^{-1}$ and $K_{An} = 5 \times 10^{-3}$ for the anode and $K_{Ca} = 5 \times 10^{-5}$ and $K_{Ca} = 5$ for the cathode. The stoichiometric coefficients are $s_F = 1$, $s_O = 1$, $s_C = 6$, and the number of electrons involved in the kinetic reaction (n) is 6. The inlet velocity profile for each inlet is set to the steady state flow profile for a rectangular duct with $V_{\max} = 5$ and $\Gamma = 4 \times 10^{-5}$. The diffusion coefficient for the neutral species is less than the diffusion coefficient of the cation by an order of magnitude $\beta_F = \beta_O = 1/10$ and the inlet concentration ratios are $\gamma_F = \gamma_O = 1$. The Stern layer capacitance is $C_s = 80\,\mu F/\text{cm}^2$ and the Stern layer permittivity is 10 times that of the permittivity in a vacuum.

Neutral Species Distribution

The concentration distributions for the neutral species are shown in Figure 4. The results for the full domain are shown as contour plots in Figures 4*a* and 4*b* for

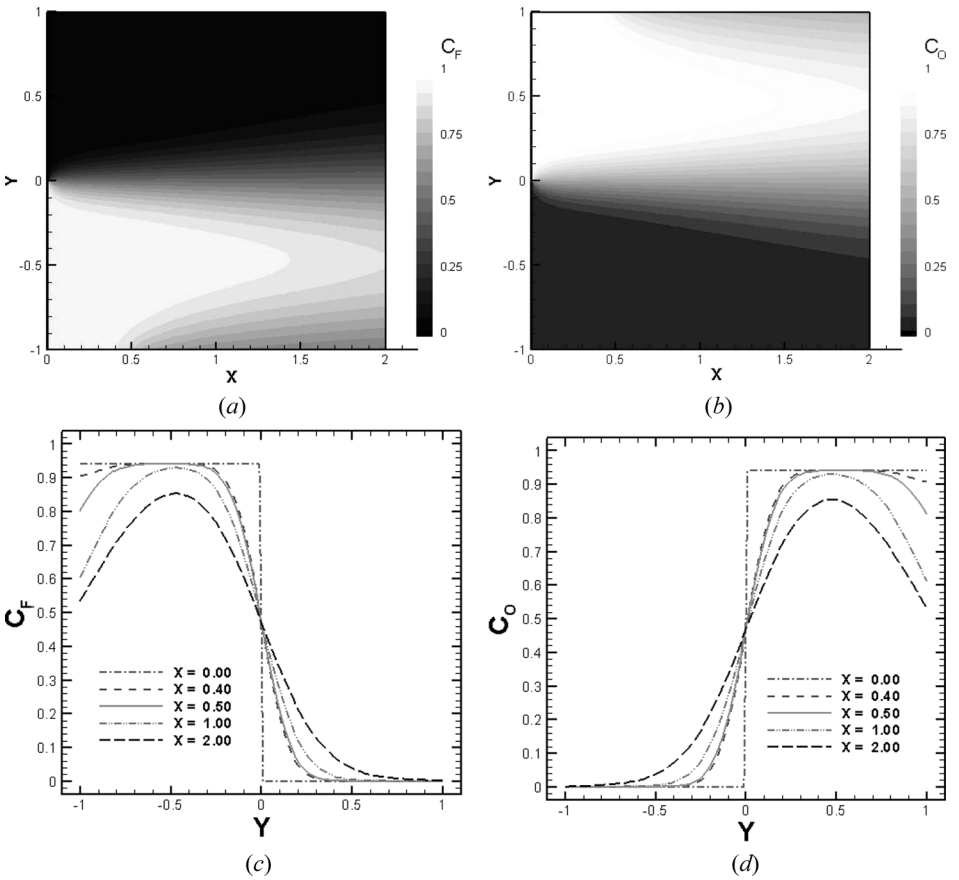

Figure 4. Concentration distributions for the neutral species. The contour plots show the results for the entire domain for (*a*) fuel and (*b*) oxidant. Concentration distribution across the channel at few specific locations along the channel for (*c*) fuel and (*d*) oxidant.

fuel and oxidant, respectively. The formation of a depletion boundary layer can be seen near the anode ($Y \rightarrow -1$) in Figure 4*a* and close to the cathode ($Y \rightarrow 1$) in Figure 4*b*. The boundary layer starts at the upstream side of the electrode. As the fuel and oxidant are consumed by the electrode kinetics, they are depleted from the fluid. The further downstream of the cell, the more reactants have been consumed. If the current is large enough that all the reactants at the electrode are consumed and cannot be replenished by diffusion from the bulk flow, the kinetics for that electrode will become transport limited. These figures also show that fuel and oxidant remain mostly unmixed in the channel. At the channel inlet (in Figure 4*a*), the fuel is specified to the inlet concentration for the entire fuel inlet, and not present at the oxidant inlet. As the flow progresses downstream the fuel begins to diffuse into the oxidant side. This is known as transverse diffusional mixing and is more readily seen in Figure 4*c* for fuel and Figure 4*d* for the oxidant. If the concentration of fuel at the cathode increases above zero it can oxidize there, effectively short circuiting the fuel cell. This is known as fuel crossover and it can be very detrimental to fuel cell performance. In a LFFC, there is no physical separation between the anode and the cathode; fuel crossover is prevented by controlling the operating parameters such that the separation of neutral species is maintained. This behavior cannot be captured by previous electrochemical models that include EDL that are only 1-D. For computational simplicity, the length of the channel was kept rather small compared to the height of the channel. If the channel length were increased, the amount of cross channel diffusion between the two neutral streams would increase until they are fully mixed at a very long channel length.

Electrolyte Potential

The potential distribution in the electrolyte for the full domain is shown in Figure 5*a*. The EDL shape matches expected results in the cross channel direction. The results presented in Figure 5*b* are the same as those presented in the contour plot but show the behavior of the potential across the channel for different positions along the channel. The potential drop across the channel, especially in the bulk fluid (away from the electrodes), can clearly be seen. Further downstream, the potential drop becomes more linear. However, according to the 1-D analytical solution, it will never become linear when current across the cell is present [26]. Therefore, increasing the channel length would not have an impact on the potential in the electrolyte. This potential drop is known as the cell's internal resistance in the fuel cell community. The potential distribution across the channel at the inlet is not flat as shown in Figures 5*a* and 5*b*. This is because the upstream potential is influenced by the potential distribution between the electrodes. If the distance between the inlet and the start of the electrodes was large enough then the potential distribution at the inlet would be flat. The inset in Figure 5*b* shows the potential distribution near the (anode) electrode. The evolution of the EDL at the electrode is very quick and the potential distribution reaches a stable shape just downstream of the start of the electrode; so if the channel length were increased the shape of the EDL wouldn't change. Also the lack of a double layer at the insulated wall ($X = 0$, $X = 0.4$) can be seen in the inset of Figure 5*b*. The developing behavior of the EDL along a channel cannot be captured by 1-D results. Also, a 2-D solution yields the shape of the double layer

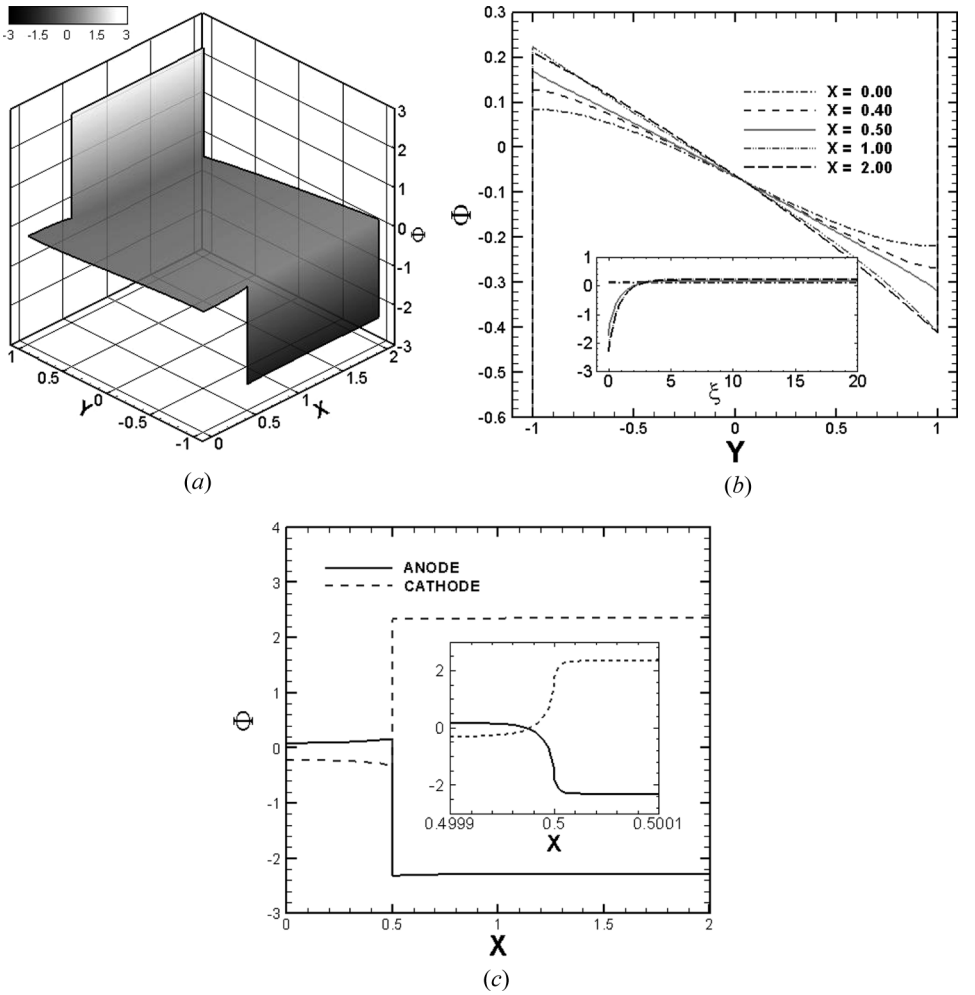

Figure 5. Distribution of potential in the electrolyte for the case of $\Phi_{An} = -3$, $\Phi_{Ca} = -3$. The (*a*) contour plots show the results for the entire domain and (*b*) specific cross channel results for different locations along the channel. The inset in (*b*) shows the near wall potential distribution against the inner scale. The potential distribution along the entire channel is shown in (*c*) for the anode and cathode and specifically at the inception of the electrodes ($X = 0.5$) in the inset figure.

along the channel at the beginning of the electrode (Figure 5*c*) which, to our knowledge, has not been presented before.

Ion Distribution

The concentration distributions of the ions are presented in Figure 6. Figure 6*a* shows the concentration distribution of the cation. The positively charged cations are attracted towards the anode electrode which is negatively charged. As the fuel oxidizes in the anodic side, positively charged cations are released into the electrolyte and negatively charged electrons are transferred into the electrode. These electrons

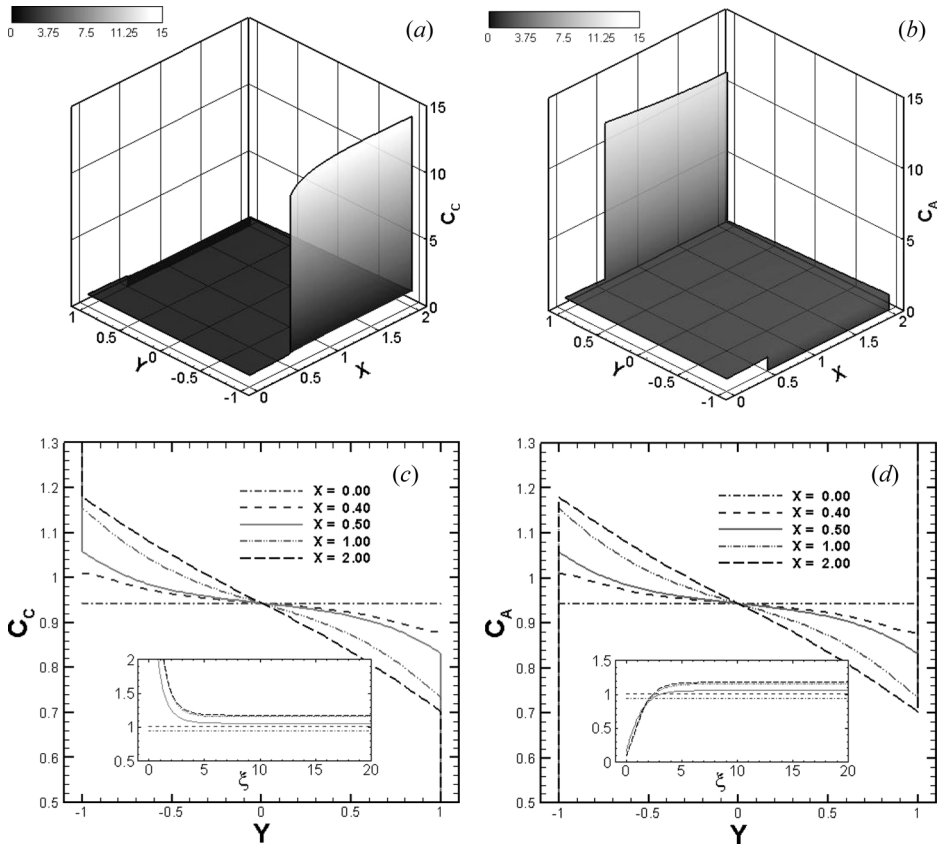

Figure 6. Concentration distributions for the ions. The contour plots show the results for the entire domain for (*a*) cation and (*b*) anion. Specific cross channel results are also shown for (*c*) cation and (*d*) anion at different locations along the channel. The insets in (*c*) and (*d*) show the near wall concentration distribution against the inner length scale.

build up causing a net negative charge in the anode. The opposite phenomenon occurs in the cathodic side, where electrons are consumed from the electrode and combined with cations in the electrolyte. The electron depletion from the cathode electrode results in a net positive charge in the cathode electrode. This positive charge repels the cations resulting in depletion of cations in the electrolyte at the cathodic side. Similarly but opposite for the anion, shown in Figure 6*b*, where there is a depletion of anions at the anode and a buildup of anions at the cathode in the electrolyte.

Consider the anodic side in Figures 6*a* and 6*b*; the local increase in cation concentration is greater than the local decrease in anion, which is consistent with EDL theory. The net charge in the EDL must be equal and opposite to the net charge in the solid electrode. However, the anion concentration can only decrease to zero near the electrode so the remaining difference must be accounted for by a larger excess of cations. Figures 6*c* and 6*d* show the distribution of the cation and anion, respectively, across the channel; in the bulk fluid regions (away from the electrodes), the electroneutrality condition holds. It can be seen that the shape

of the anion and cation distribution follows closely the shape of the potential distribution. This is a direct result of the strong coupling between the potential and ion distributions. This distribution of ions throughout the domain cannot be properly captured by models that neglect the coupling between potential and ion transport. A very interesting observation is apparent in Figure 6*a*, where the concentration of cations near the anode increases as the fluid progresses downstream. Similarly, the concentration of anions at the cathode in Figure 6*b* decreases. Although the EDL develops quickly at the beginning of the electrode, the concentration distribution of the ions continues to develop downstream as evidenced by the insets in Figures 6*c* and 6*d*. The insets show the near electrode distribution of the cation and anion at the anodic side as a function of the inner length scale. The distribution at $X = 1.00$ and $X = 2.00$ are similar and show that the concentrations are indeed stabilizing and appear to no longer be changing in the downstream direction. Therefore, one would expect the shape of the ion distribution in the EDL to remain constant to those at the outlet if the channel length were increased.

Fluid Velocity Profile

The magnitude of the velocity distribution is shown in Figure 7. Clearly visible is the velocity profile at the inlet as a result of two feed channels merging as described earlier. The flow in the channel is a developing flow as the two inlet streams merge into a single channel flow. The results show that the flow can be assumed to be fully developed for $x_{out} = 2L$ and the results at the exit of the channel would not change if the channel length were increased. The velocity profile determines the advection

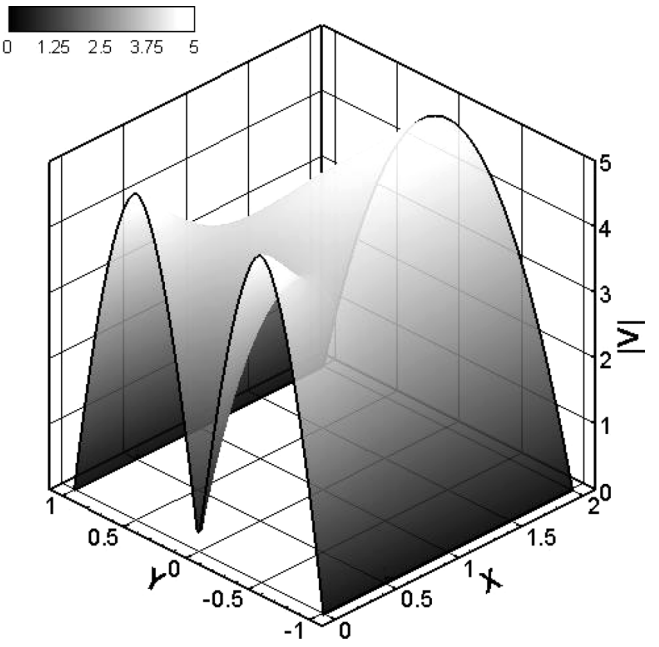

Figure 7. Contour plot of velocity magnitude profile.

of the neutral species and ions, which has been neglected in previous EDL fuel cell studies. Figures 8*a* and 8*b* shows the corresponding pressure plot where a dramatic increase in pressure in the EDL region can be seen. This is the osmotic pressure that develops due to the EBF in an equilibrium EDL [35]. The near wall fluid flow is affected by the EBF, but primarily at the start of the electrode. From Figures 8*c* and 8*d* it is clear that the velocity profile only at the start of the electrodes ($X = 0.5$) shows an appreciable deviation from the expected velocity profile. The insets in Figures 8(*b*)–(*d*) show the near wall nature of flow and pressure. The inset figures for velocity components (Figures 8*c* and 8*d*) show that the velocity at the wall remains zero because of the no-slip and no-penetration boundary conditions.

The EDL presented in this work can be thought of as an equilibrium EDL plus a small deviation that is a result of the cross channel current. It is important to note that an equilibrium EDL cannot produce flow because of the osmotic pressure [35].

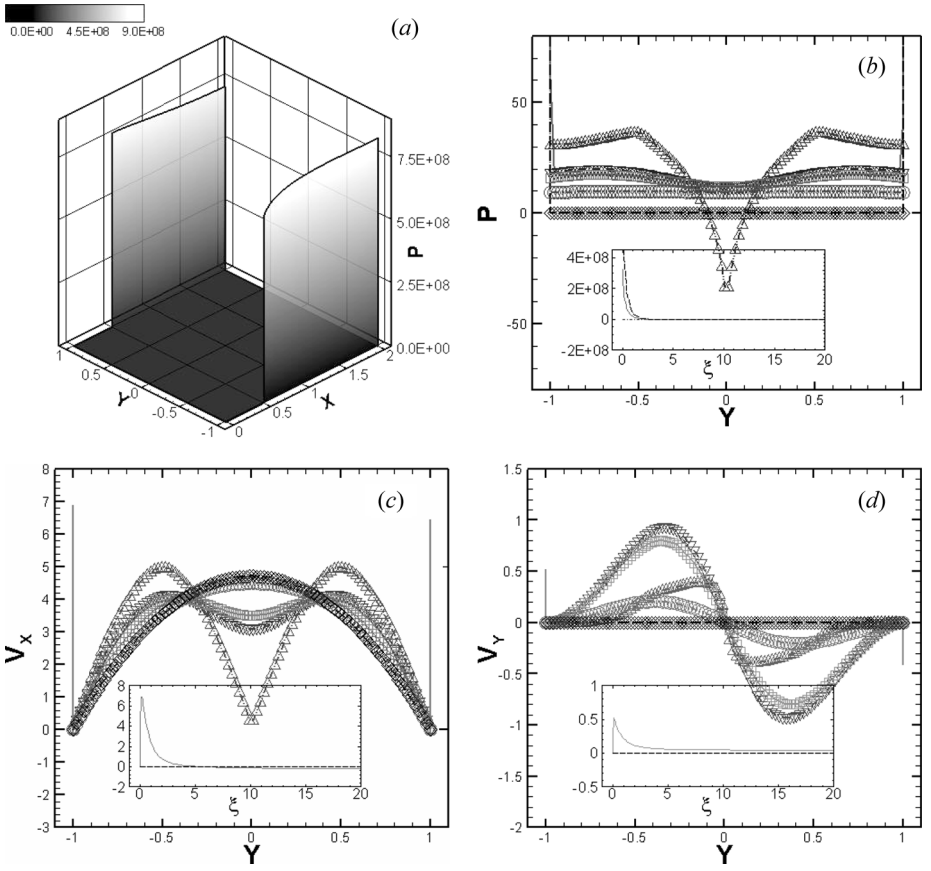

Figure 8. (*a*) Contour plot of pressure throughout the computational domain. Comparison of (*b*) cross channel pressure and (*c*) and (*d*) flow results with the electric body force term (case 1: Lines) and without (case 2: Symbols). The cross channel distributions of pressure and velocity are shown at different positions along the channel (–·–·– △: $X = 0.00$, – – – – ▽: $X = 0.40$, –··–□: $X = 0.50$, ——○: $X = 1.00$, – – –◇: $X = 2.00$). The insets in (*b*)–(*d*) show the near wall distributions against the inner length scale.

In other words, the part of the EDL that is in equilibrium does not affect flow. Only the slight deviation from the equilibrium EDL caused by the current density will affect flow. Figures 8*b–d* also show a comparison between two cases of flow results: With the EBF (case 1) and without the EBF (case 2). In Figure 8*b*, it can be seen that the pressure for case 2 only deviates from case 1 near the wall where the osmotic pressure is active. The fluid velocity in case 2 for the streamwise direction (Figure 8*c*) and cross-channel direction (Figure 8*d*) only deviate from case 1 near the wall at the start of the electrodes. By comparing the numerical results for electrolyte potential and concentration distributions (not shown) for cases 1 and 2, it was found that the EBF has a very negligible effect in the electrochemical results. For instance, neglecting the EBF from the system of equations causes a maximum change of 5×10^{-4} in potential at any point in the domain, which is four orders of magnitude less than the electrode potential. For the concentration distributions, the maximum change at any point is 5×10^{-3}, which is three orders of magnitude lower than the electrolyte concentration. Given the negligible differences in the electrochemical (electrolyte concentration and potential) results between two cases, it can be concluded that the EBF can be neglected from the momentum equations of LFFC model. However, the inclusion of EBF provides interesting flow and pressure results near the wall and electrode regions.

Cell Performance

Two important parameters to evaluate fuel cell performance are cell potential and current density. The cell potential can be calculated as $\Psi_{\text{cell}} = \Psi_{Ca} - \Psi_{An}$

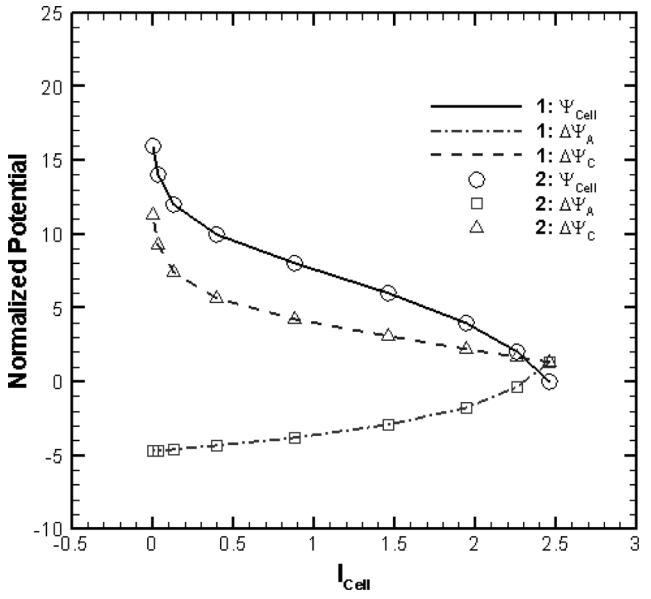

Figure 9. Voltage-Current plots for the laminar flow fuel cell comparing results with (case 1) and without (case 2) the EBF. Shown is the total cell voltage, $\Psi_{\text{cell}} = \Psi_{Ca} - \Psi_{An}$, the anode electrode potential $\Delta\Psi_A = (\Psi_A - \Phi_{Y=0})$, and the cathode electrode potential $\Delta\Psi_C = (\Psi_C - \Phi_{Y=0})$.

using the input electrode potentials, and the cell current density can be calculated by integrating the current density along one of the electrodes

$$I_{An} = \frac{1}{(X_{\text{out}} - X_{El})} \int_{X_{El}}^{X_{\text{out}}} J_{An}(X) dX \tag{13}$$

A positive cell current correlates a positive anode current and a negative cathode current by convention. If the governing equations and accompanying boundary conditions are solved for different values of $\Psi_{\text{cell}}(\Psi_{\text{An}}, \Psi_{\text{Ca}})$ ranging from zero (short circuit) up until $I_{\text{cell}} = 0$ (open circuit) then a classic fuel cell analysis plot, the voltage-current plot, can be created. Figure 9 shows a V-I plot for a fuel cell operating at the same kinetic and flow parameters and EBF cases described above. The anode electrode potential $\Delta\Psi_A = (\Psi_A - \Phi_{Y=0})$ and cathode electrode potential $\Delta\Psi_C = (\Psi_C - \Phi_{Y=0})$ are also shown in Figure 9. For the anode, the more negative the electrode potential, the lower the current density. The opposite is the true for the cathode, i.e., the more positive the electrode potential the lower the current density. Figure 9 shows that the cell is anode limited when operating as a short circuit, i.e., the anode electrode potential is less negative than the cathode electrode potential is positive. However, at open circuit, the cathode electrode potential is greater than the anode electrode potential and the cell is cathode limited. Also shown in Figure 9 is a comparison of LFFC performance results between the two cases: with (case 1) and without (case 2) the EBF term. The results clearly show that the EBF produces no noticeable effect on the device level results. This is due to the fact that the primary impact of the EBF on fluid flow is at a very small region at the start of each electrode. Any change in kinetic performance in this location is insignificant when compared to the kinetic performance of the entire electrode.

CONCLUSION

A 2-D numerical model is developed for a laminar flow fuel cell considering ion transport and EDL around the electrodes, and validated against published analytical results. Finite volume method is used to form algebraic equations from governing partial differential equations. The numerical solution was obtained using Newton's method for a system of equations and a block TDMA solver. Different operating phenomena such as the laminar flow separation, the development of the depletion boundary layers and EDL, and the coupling of ion transport with electric potential were shown. The model was also able to show the shape of the EDL in the downstream direction as well as how the double layer changes along the electrode. These numerical results demonstrate the model's ability to capture the complex behavior of such a device. A comparison of results with and without the EBF in the momentum conservation equations revealed that the EBF had only a minor effect on fluid flow and the potential and concentration distributions. This minor effect yielded a negligible difference in LFFC performance and therefore it is possible to neglect the EBF term from the momentum conservation equation of LFFC model. If the EBF term is neglected from the momentum conservation equations, the flow field becomes decoupled from the PNP equations and the complexity of the LFFC model reduces

significantly. Future works based on this model may further probe the depths of the complex electrochemical system of laminar flow fuel cells.

REFERENCES

1. J. Larminie and A. Dicks, *Fuel Cell Systems Explained*, 2nd ed., Wiley, West Sussex, UK, 2003.
2. J. O. Bockris, A. K. N. Reddy, and M. Gamboa-Aldeco, *Modern Electrochemistry 2A: Fundamentals of Electrodics*, 2nd ed., pp. 1035–1074, Kluwer Academic/Plenum Publishers, New York, 2000.
3. E. Carcadea, H. Ene, D. B. Ingham, R. Lazar, L. Ma, M. Pourkashanian, and I. Stefanescu, A Computational Fluid Dynamics Analysis of a PEM Fuel Cell System for Power Generation, *Int. J. Numer. Meth. for Heat & Fluid Flow*, vol. 17, pp. 302–312, 2007.
4. P. K. Das, X. Li, and Z. -S. Liu, Analytical Approach to Polymer Electrolyte Memebrane Fuel Cell Performance and Optimization, *J. Electroanalytical Chemistry*, vol. 604, pp. 72–90, 2007.
5. S. Um, C. -Y. Wang, and K. S. Chen, Computational Fluid Dynamics Modeling of Proton Exchange Membrane Fuel Cells, *J. the Electrochemical Society*, vol. 147, pp. 4485–4493, 2000.
6. C.-Y. Wang, Fundamental Models for Fuel Cell Engineering, *Chem. Rev.*, vol. 104, pp. 4727–4766, 2004.
7. A. Z. Weber and J. Newman, Modeling Transport in Polymer-Electrolyte Fuel Cells, *Chem. Rev.*, vol. 104, pp. 4679–4726, 2004.
8. J. D. Morse, Micro-Fuel Cell Power Sources, *Int. J. Energy Res.*, vol. 31, pp. 576–602, 2007.
9. R. Ferrigno, A. D. Stroock, T. D. Clark, M. Mayer, and G. M. Whitesides, Membraneless Vanadium Redox Fuel Cell Using Laminar Flow, *J. Am. Chem. Soc.*, vol. 124, pp. 12930–12931, 2002.
10. E. R. Choban, L. J. Markoski, A. Wieckowski, and P. J. A. Kenis, Microfluidic Fuel Cell based on Laminar Flow, *J. Power Sources*, vol. 128, pp. 54–60, 2004.
11. E. R. Choban, P. Waszczuk, and P. J. A. Kenis, Characterization of Limiting Factors in Laminar Flow Based Membraneless Microfuel Cells, *Electrochemical and Solid-State Letters*, vol. 8, pp. A348–A352, 2005.
12. I. B. Sprague, P. Dutta, and S. Ha, Characterization of a Membraneless Direct-Methanol Micro Fuel Cell, *Proc. IMechE Part A: J. Power and Energy*, vol. 223, pp. 799–808, 2009.
13. R. S. Jayashree, L. Gancs, E. R. Choban, A. Primak, D. Natarajan, L. J. Markoski, and P. J. A. Kenis, Air-Breathing Laminar Flow-Based Microfluidic Fuel Cell, *J. Am. Chem. Soc.*, vol. 127, pp. 16758–16759, 2005.
14. R. S. Jayashree, D. Egas, J. S. Spendelow, D. Natarajan, L. J. Markoski, and P. J. A. Kenis, Air-Breathing Laminar Flow-Based Direct Methanol Fuel Cell with Alkaline Electrolyte, *Electrochemical and Solid-State Letters*, vol. 9, pp. A252–A256, 2006.
15. E. Kjeang, J. McKechnie, D. Sinton, and N. Djilali, Planar and Three-Dimensional Microfluidic Fuel Cell Architectrues based on Graphite Rod Electrodes, *J. Power Sources*, vol. 168, pp. 379–390, 2007.
16. E. Kjeang, R. Michel, D. A. Harrington, N. Djilali, and D. Sinton, A Microfluidic Fuel Cell with Flow-Through Porous Electrodes, *J. Am. Chem. Soc.*, vol. 130, pp. 4000–4006, 2008.
17. A. Bazylak, D. Sinton, and N. Djilali, Improved Fuel Utilization in Microfluidic Fuel Cells: A Computational Study, *J. Power Sources*, vol. 143, pp. 57–66, 2004.
18. S. K. Yoon, G. W. Fichtl, and P. J. A. Kenis, Active Control of the Depletion Boundary Layers in Microfluidic Electrochemical Reactors, *Lab Chip*, vol. 6, pp. 1516–1524, 2006.
19. M. -H. Chang, F. Chen, and N. -S. Fang, Analysis of Membraneless Fuel Cell Using Laminar Flow in a Y-shaped Microchannel, *J. Power Sources*, vol. 159, pp. 810–816, 2006.

20. F. Chen, M.-H. Chang and C.-W. Hsu, Analysis of Membraneless Microfuel Cell using Decomposition of Hydrogen Peroxide in Y-shaped Microchannel, *Electrochimica Acta*, vol. 52, pp. 7270–7277, 2007.
21. F. Chen, M. -H. Chang, and M. -K. Lin, Analysis of Membraneless Formic Acid Microfuel Cell using a Planar Microchannel, *Electrochimica Acta*, vol. 52, pp. 2506–2514, 2007.
22. M. Z. Bazant, K. T. Chu, and B. J. Bayly, Current-Voltage Relations for Electrochemical Thin Films, *Siam J. Appl. Math.*, vol. 65, pp. 1463–1484, 2005.
23. K. T. Chu and M. Z. Bazant, Electrochemical Thin Films At and Above the Classical Limiting Current, *Siam J. Appl. Math.*, vol. 65, pp. 1485–1505, 2005.
24. Z. Chen and R. K. Singh, General Solution for the Poisson-Boltzman Equation in Semininfinte Planar Symmetry, *J. Colloid and Interface Sci.*, vol. 245, pp. 301–306, 2002.
25. W. D. Murphy, J. A. Manzanares, F. Mafe, and H. Reiss, A Numerical Study of the Equilibrium Diffuse Double Layer in Electrochemical Cells, *J. Phys. Chem.*, vol. 96, pp. 9983–9991, 1992.
26. A. Bonnefont, F. Argoul, and M. Z. Bazant, Analysis of Diffuse-layer Effects on Time-Dependent Interfacial Kinetics, *J. Electroanalytical Chem.*, vol. 500, pp. 52–61, 2001.
27. M. van Soestbergen, P. M. Biesheuvel, and M. Z. Bazant, Diffuse-Charge Effects on the Transient Response of Electrochemical Cells, *Phys. Rev. E*, vol. 81, pp. 021503-1–021503-13, 2010.
28. P. M. Biesheuvel, M. van Soestbergen, and M. Z. Bazant, Imposed Currents in Galvanic Cells, *Electrochimica Acta*, vol. 54, pp. 4857–4871, 2009.
29. M. van Soestbergen, Diffuse Layer Effects on the Curren in Galvanic Cells Containing Supporting Electrolyte, *Electrochmica Acta*, vol. 55, pp. 1848–1854, 2010.
30. P. M. Biesheuvel, A. A. Franco, and M. Z. Bazant, Diffuse Charge Effects in Fuel Cell Membranes, *J. the Electrochemical Society*, vol. 156, pp. B225–233, 2009.
31. A. U. Modak and M. T. Lusk, Kinetic Monte Carlo Simulation of a Solid-Oxide Fuel Cell: I. Open Circuit Voltage and Double Layer Structure, *Solid State Ionics*, vol. 176, pp. 2181–2191, 2005.
32. P. Dutta, A. Beskok, and T. C. Warburton, Numerical Simulation of Mixed Electroosmotic/Pressure Driven microflows, *Numer. Heat Transfer A*, vol. 41, pp. 131–148, 2002.
33. J. Shim, P. Dutta, and C. F. Ivory, Finite Volume Methods for Isotachophoretic Separation in Microchannel, *Numer. Heat Transfer A*, vol. 52, pp. 441–461, 2007.
34. S. Acharya, B. R. Baliga, and K. Karki, Pressure-Based Finite-Volume Methods in Computational Fluid Dynamics, *J. Heat Transfer-Transactions of the ASME*, vol. 129, pp. 407–424, 2007.
35. H. -C. Chang and L. Y. Yeo, *Electrokinetically-Driven Microfluidics and Nanofluidics*, pp. 39–40, Cambridge University Press, New York, 2010.
36. www.OpenMP.org. (accessed 20 October 2009).
37. J. Shim, P. Dutta, and C. F. Ivory, Parallel Implementation of Finite Volume Based Method for Isoelectric Focusing, *J. Mechanical Sci. and Tech.*, vol. 23, pp. 3169–3178, 2009.

APPENDIX 1: NUMERICAL FORMULATION

The system of equations used to describe electrochemical system (Eqs. (3) and (4)) is nonlinear and highly coupled. Therefore, application of finite-volume method yields a set of nonlinear algebraic equations that are not straightforward to solve, and cannot be solved with tridiagonal matrix algorithm (TDMA) or Gauss-Seidel methods often used in conjunction with the finite volume method. Here, Newton's method is applied for a system of equations, which offers two

distinct advantages. First, all the transport equations and the Poisson's equation can be solved simultaneously, a necessity due to their strongly coupled nature. Second, that Newton's method converts nonlinear system of algebraic equations to a linear set.

In order for Newton's method to be applied, the Jacobian matrix must first be obtained. For our case, the system of finite volume equations can be written as

$$f(\vec{s}) = 0 \tag{14}$$

where f is a set of $5m$ algebraic equations, 5 being the number of unknown fields (Φ, C_C, C_A, C_F, and C_O) and m the number of finite control volumes ($f \in \mathbb{R}^{5m}$). The unknown vector is given by $\vec{s}$ and the Jacobian matrix of the system is

$$J(\vec{s}) = \frac{\partial f}{\partial \vec{s}} \tag{15}$$

Now, Newton's method for a system of algebraic equations becomes

$$J(\vec{s}_i)\vec{\eta}_i = -f(\vec{s}_i) \tag{16}$$

where i represents the current Newton iteration and $\vec{\eta}$ is used to update the unknown vector for the next iteration as

$$\vec{s}_{i+1} = \vec{s}_i + \vec{\eta} \tag{17}$$

Equation 16 is solved numerically for $\vec{\eta}$ which is then used to update the unknown vector through Eq. (17). This produces a solver with two loops: an inner and an outer loop. The outer loop is the Newton iteration, while the inner loop is the iterative solver for Eq. (16). To solve the inner loop, it is important to look at the structure of the Jacobian, which is a sparse matrix. For simplicity in explanation, a 3×3 grid of finite volumes is considered with three unknown fields, A, B, and C which gives nine control volumes and a set of 27 equations. If the ordering of the unknown vector is

$$\begin{bmatrix} A_1 \\ \vdots \\ A_9 \\ \mathrm{B}_1 \\ \vdots \\ \mathrm{B}_9 \\ C_1 \\ \vdots \\ C_9 \end{bmatrix} \tag{18a}$$

Then, the structure of the nonzero values in the Jacobian matrix is shown by Eq. (18*b*).

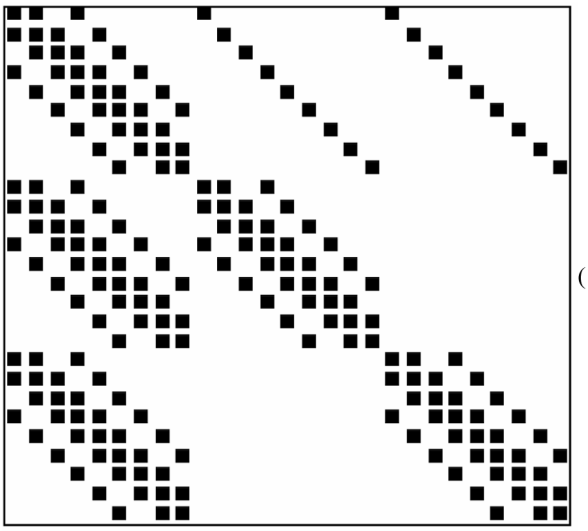

(18*b*)

This matrix is asymmetric and cannot be solved with simple numerical solution techniques. However, if the ordering of the unknown vector is

$$\begin{bmatrix} \phi_1 \\ A_1 \\ B_1 \\ \vdots \\ \phi_9 \\ A_9 \\ B_9 \end{bmatrix} \tag{19a}$$

Then, the structure of the nonzero values in the Jacobian matrix can be arranged as

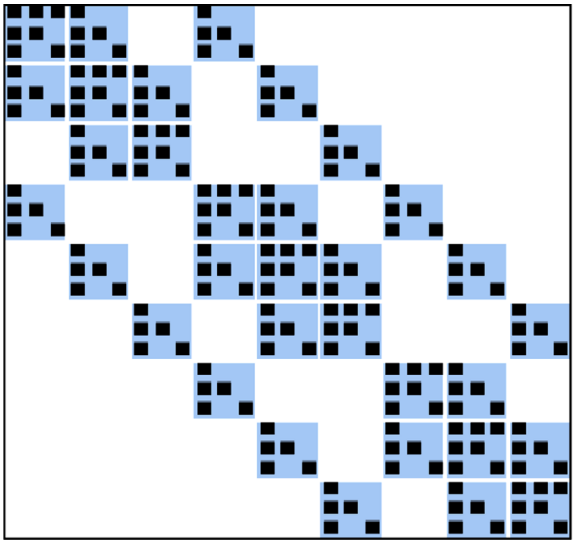

(19*b*)

The matrix is still asymmetric; however, it is block symmetric as suggested by the larger lighter blocks in Eq. (19*b*). This block structure of the Jacobian is similar to the point structure of a system with one governing equation and a single unknown parameter. Therefore, the block structure of the Jacobian in Eq. (19*b*) can be solved with a Block TDMA. The Block TDMA requires the solution of multiple block equations. Since the block sizes are small, in this example 3×3, these equations can be solved rather quickly using LU decomposition.

Another advantage of a block TDMA is that it is relatively straightforward to implement in a parallel environment. The implementation in this work uses the OpenMP API which allows for parallel processing on multiple shared memory processors [36]. Figure 10*a* shows the process flow through an OpenMP parallel region. The program initiates as a single thread, the master thread, and progresses serially until the inner solution loop where a fork is encountered. In OpenMP, a fork is

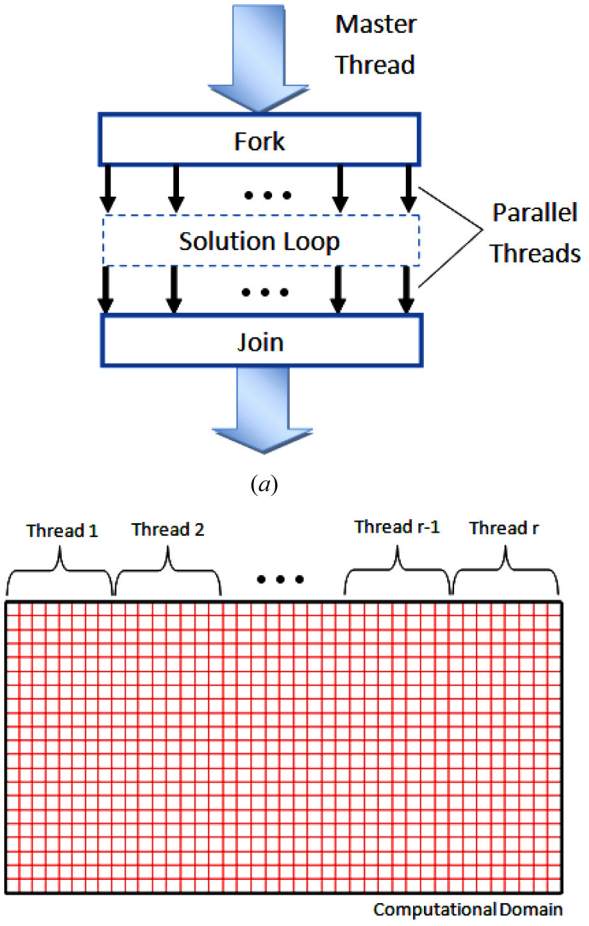

Figure 10. Parallelization scheme for laminar flow fuel cell. (*a*) The computational flow of a single master thread dividing into multiple parallel threads at a fork and condensing back to the master thread at a join; and (*b*) the computational domain is decomposed into sub-domains that can be distributed to the individual parallel threads.

the start of a parallel region. At a fork the domain is decomposed into r sub-domains that are distributed amongst r parallel processes as shown in Figure 10*b* [37]. At a fork the master thread becomes a group of r equivalent parallel threads that each contains a unique solution loop for their specific sub-domain. Because the processors have a shared memory bank, parameters can be shared between the threads, such as the unknown vector $\vec{s}$ or update vector $\vec{\eta}$. This means that each thread is able to access the most current value of the unknown vector and update vector for the entire domain while operating on its unique sub-domain. At the end of each solution iteration, the threads can be synced which prevents one sub-domain to progress faster than others. By doing this, the parallel solution process is equivalent to what a serial process would be. Once convergence has been satisfied in each sub domain, the process proceeds to a join. A join is the termination of a parallel region in OpenMP where the parallel threads are released by the code except for a single thread which is retained as the master thread. There is no need for communication between the threads due to the shared memory bank which already contains the most current values. After a join, the code proceeds serially.

APPENDIX 2: NORMALIZED EQUATIONS

For general purpose use of numerical results, the governing equations are normalized. This is accomplished by selecting appropriate scale factors for the system of governing equations. The convention of this work is that lower case characters represent the dimensional values, while upper case characters represent nondimensional values. Using scale factors shown in Table 1, the normalized system of governing equations for the electrochemical cell becomes

$$\nabla \cdot (\vec{V} C_F) = \nabla \cdot (\beta_F \nabla C_F) \tag{20a}$$

$$\nabla \cdot (\vec{V} C_O) = \nabla \cdot (\beta_O \nabla C_O) \tag{20b}$$

$$\nabla \cdot (\vec{V} C_C) = \nabla \cdot (\nabla C_C + C_C \nabla \Phi) \tag{20c}$$

$$\nabla \cdot (\vec{V} C_A) = \nabla \cdot (\nabla C_A + C_A \nabla \Phi) \tag{20d}$$

$$-2\left(\frac{\lambda_D}{L}\right)^2 \nabla^2 \Phi = C_C - C_A \tag{20e}$$

where $\beta_F = D_F/D_E$ and $\beta_O = D_O/D_E$ are the ratios of the diffusion coefficient of the neutral species to the diffusion coefficient of the cation. This ratio allows for a different diffusion rates for the neutral species which are often molecules, and have diffusion coefficients an order of magnitude less than that of the ions.

The normalized momentum and mass conservation equations become

$$1/Sc(\vec{V} \cdot \nabla)\vec{V} = \nabla^2 \vec{V} - \nabla P - \Gamma(C_C - C_A)\nabla \Phi \tag{21a}$$

$$\nabla \cdot \vec{V} = 0 \tag{21b}$$

where $Sc = \frac{\mu}{\rho D_E}$ is the Schmidt number which is the ratio between momentum diffusivity and mass diffusivity and $\Gamma = \frac{\mu\omega_E}{L^2 C_E}$.

Using the normalized variables presented, the nondimensional expressions for the generalized Frumkin-Butler-Volmer equation are

$$\text{Anode} : J = n\overleftarrow{k_{An}}\,\gamma_F C_F e^{(1-\alpha)\Delta\Phi_s} - n\overrightarrow{k_{An}}\,C_C e^{-\alpha\Delta\Phi_s} \tag{22a}$$

$$\text{Cathode} : J = n\overleftarrow{k_{Ca}}\,e^{(1-\alpha)\Delta\Phi_s} - n\overrightarrow{k_{Ca}}\,\gamma_O C_O C_C e^{-\alpha\Delta\Phi_s} \tag{22b}$$

where the normalized rate constants are $\overleftarrow{k_{An}} = \overleftarrow{k_{An}} L/D_E$ and $\overrightarrow{k_{An}} = \overrightarrow{k_{An}} L/D_E$ for the anode, and $\overleftarrow{k_{Ca}} = \overleftarrow{k_{Ca}} L/C_E D_E$ and $\overleftarrow{k_{Ca}} = \overrightarrow{k_{Ca}}\, L/C_E D_E$ for the cathode. The dimensionless parameter, γ, is the ratio of the electrolyte concentration to the specified inlet concentration of the neutral species, $\gamma_F = C_E/C_{F,\text{in}}$ and $\gamma_O = C_E/C_{O,\text{in}}$. The drop across the Stern layer is normalized by the same scale factor as potential, $\Delta\Phi_s = zF\Delta\phi_s/RT$.